



Electron directed migration cooperated with thermodynamic regulation over bimetallic NiFeP/g-C₃N₄ for enhanced photocatalytic hydrogen evolution



Qiaohong Zhu^a, Bocheng Qiu^a, Huan Duan^b, Yeteng Gong^a, Zengwei Qin^a, Bin Shen^a, Mingyang Xing^{a,*}, Jinlong Zhang^{a,*}

^a Key Laboratory for Advanced Materials and Joint International Research Laboratory of Precision Chemistry and Molecular Engineering, Feringa Nobel Prize Scientist Joint Research Center, School of Chemistry and Molecular Engineering, East China University of Science and Technology, 130 Meilong Road, Shanghai 200237, PR China

^b School of Chemistry and Chemical Engineering, Southwest University, Chongqing 400715, PR China

ARTICLE INFO

Keywords:

NiFeP
g-C₃N₄
Photocatalytic hydrogen reaction
Electron migration

ABSTRACT

Bimetallic phosphides have attracted considerable attention in photocatalytic hydrogen evolution reaction (HER), owing to its thermodynamic feasibility. Most reports attributed the HER activity to the reduction of free energy of protonation (ΔG_{H^+}), however, few revealed the whereabouts of the photo-induced electrons, which makes the mechanism of HER not very clear. Herein, nickel-iron bimetallic phosphide (NiFeP) is designed onto graphitic carbon nitride (NiFeP/g-C₃N₄) for the photocatalytic HER, which exhibits a high hydrogen production of 3.549 mmol g⁻¹ h⁻¹. It is found that the co-catalyst of NiFeP can not only reduce the ΔG_{H^+} , but also make the photogenerated electrons transfer directionally, which play a synergistic role in enhancing the activity of HER. The reduction of ΔG_{H_2O} and ΔG_{H^+} over NiFeP in HER can be well demonstrated by the density functional theory (DFT) calculations. Furthermore, the localized distribution of electrons on the surface of NiFeP is verified by measuring the lifetime of photo-generated carriers combined with the REDOX experiment. The shortened lifetime τ , decreased τ_1 and τ_2 of NiFeP/g-C₃N₄ indicate that the photoexcited electrons of g-C₃N₄ are directly transferred to the co-catalyst surface, contributing to the worse delocalization capacity of electrons on the catalyst and its easier reactions with protons trapped on the co-catalyst surface. Furthermore, the degradation with peroxymonosulfate (PMS) confirms the photogenerated holes over 5NiFeP/g-C₃N₄ are mainly concentrated on the surface of g-C₃N₄ to decompose H₂O for the generation of ·OH, while the photogenerated electrons are directed to the NiFeP to react with the neighboring PMS or protons to form SO₄²⁻ or H₂. Besides, the density of state intensity (DOS) also confirms the photogenerated electron migration pathway at the metal-semiconductor (NiFeP-g-C₃N₄) interface. Our research clarifies the mechanism of bimetallic phosphides co-catalytic HER system, which will provide theoretical guidance for the design and preparation of multi-metallic center photocatalytic system with a higher HER activity in the future.

1. Introduction

The development of bimetal-based catalysts, especially the earth-abundant and low-cost transition metal compounds, such as NiCoP [1,2], NiCoO [3,4], MoFeS [5], NiFeP [6,7], FeNiSe [8], Ni₃FeN [9], is essential in the field of hydrogen evolution reaction (HER) and oxygen evolution reaction (OER). For electrocatalysis, the mechanism of metallic sulphides or phosphides for the HER is mainly to the reduction of Gibbs free energies for hydrogen adsorption and H₂ formation [10–15]. However, to the photocatalysis, metal sulphides or phosphides are often employed as the co-catalysts, besides thermodynamic regulation, the

whereabouts of photogenerated electrons is equally important to the HER performance. Unfortunately, most reports on bimetal-based photocatalytic HER only study the Gibbs free energy of hydrogen generation through the density functional theory (DFT) calculations [16–18], and few experimental data can reveal the relationship between photon-generated carriers and co-catalyst. Recently, Guo and his co-workers declared that they could only use the first-principles simulation to investigate the geometry structure and photo-induced charge-transfer property of FeCoPO_x(NWs)-C₃N₄, owing to the limitation of experimental method in studying the relationship between performance and structure at atomic level [19].

* Corresponding authors.

E-mail addresses: minyangxing@ecust.edu.cn (M. Xing), jlzheng@ecust.edu.cn (J. Zhang).

On the other hand, among various substitutions for noble metals, the transition metals of Ni and Fe have been widely employed in the HER application, owing to their relative low toxicity and high earth storage. For instance, Long et al. [10] developed an interesting electrocatalyst of Fe-Ni sulfide ultrathin nanosheets with excellent HER activity and stability in strong acidic solutions, lending an attractive alternative to the Pt catalyst. Huang et al. [6] reported Fe-tuned Ni₂P electrocatalysts with controllable morphology and structure by regulating atomic ratio of Ni/Fe, and revealed the Fe species-modulated electronic state behaviors and -boosted catalytic activity for water splitting. Recently, Xu et al. [20] prepared a polyhedrons of C,N-co-doped Fe₂P/Ni₂P (CN/FeNiP) as the co-catalysts to modify g-C₃N₄ for photocatalytic HER under visible-light irradiation, which exhibited a very high hydrogen production yield of 13.81 mmol g⁻¹ h⁻¹ but a relatively low stability under the help of Eosin Y sensitization. Although many researchers have found that the Fe-Ni bimetallic phosphatides or sulfides are ideal HER catalysts/co-catalysts in HER, most reports only focus on the synthesis of materials and the pursuit of the yield of hydrogen production without in-depth studies on the reaction mechanism. Especially, the photo-electrons migration pathway inside the intrinsic catalytic/co-catalytic activities and the reduced reaction activation energy for HER, have not been very clear. There is thereby an urgent need but it is still a significant challenge to reveal the cooperation between photogenerated electrons migration and thermodynamic regulation over bimetallic center co-catalyst in the photocatalytic HER.

Herein, we realize the development of bimetallic NiFeP co-catalyst and their properties in combination with the non-metal semiconductor g-C₃N₄ for the photocatalytic HER performance. Enabled by the doping of Fe atoms into Ni₂P structure, the modulated electronic structure (electron attractor) and the reduced energy barriers (ΔG_{H2O} and ΔG_{H^*}) can largely facilitate the HER performance. We use the decomposition experiment of peroxyomonosulfate (PMS) combined with the time-resolved fluorescence decay spectra to reveal the migration direction of photo-generated electrons. The density of state intensity from density function theory (DFT) calculations also confirms the photogenerated electron migration pathway. Simultaneously, the DFT calculations are also employed to study the thermodynamics of HER. It is demonstrated that the photo-generated electrons concentrated on bimetallic centers can transfer to the H^{*} intermediate adsorbed on phosphorus atoms to generate H₂, representing a steady cycle of the electron migration. The direct electron migration pathway, together with the electron trapping step resulting from the cyclic electron transmission capacity of NiFeP, accelerate the charge separation and increase the concentration of electrons directly involved in the activation of H^{*} for the hydrogen production. The efficiency of bimetallic phosphide assisted photocatalytic system has been remarkably improved with the apparent quantum yield (AQY) of 4.98% at 420 nm compared to that of co-catalysts/g-C₃N₄ reported.

2. Experimental section

2.1. Chemical materials

All of the reagents were used without further purification. Melamine at 99.0% purity, ammonium chloride at 99.5% purity, and triethanolamine (AR) were supplied by General-reagent (Shanghai, China). Hexamethylenetetramine at 99.0% purity and sodium hypophosphite at 99.0% purity were purchased from Aladdin (Shanghai, China). Nickel nitrate hexahydrate (AR) and Iron nitrate nonahydrate (AR) were obtained from Sinopharm Chemical Reagent Co. Ltd. (Shanghai, China). Deionized water with conductivity of 18.25 MΩ cm was used as solvent in the all experiments.

2.2. Synthesis of graphitic carbon nitride (g-C₃N₄)

Briefly, the pristine g-C₃N₄ was prepared through a simple thermal

polymerization of melamine and ammonium chloride in a muffle furnace with the heating temperature at 550 °C for 4 h, with the heating rate of 2 °C/min. Before the calcination, the two precursors should be grinded evenly in a mortar.

2.3. Preparation of NiFe(OH)₂/g-C₃N₄ hybrids

In a typical synthesis, the uniformly mixed aqueous solution of calculated nickel nitrate hexahydrate, iron nitrate nonahydrate, and hexamethylenetetramine (HMT, a typical hydrolysis agents, which can release hydroxyl ions at elevated temperature [21]) was dropwise added into the aqueous suspension of g-C₃N₄ (2.5 mg/mL). The mixture was kept at 90 °C for 6 h under stirring. Afterwards, the products were washed with deionized water and ethanol for several times, and finally freeze-dried at -60 °C.

2.4. Preparation of NiFeP/g-C₃N₄ photocatalysts

In the single-step phosphatization process [22], 50 mg of the obtained materials and 0.5 g sodium hypophosphite were placed in the tube furnace with the temperature of 300 °C for 2 h in the N₂ atmosphere. Samples with different loading contents of NiFeP (1, 2.5, 5, 7.5, 10 wt%) were named as 1NiFeP/g-C₃N₄, 2.5NiFeP/g-C₃N₄, 5NiFeP/g-C₃N₄, 7.5NiFeP/g-C₃N₄, 10NiFeP/g-C₃N₄, respectively. The synthesis of Ni₂P/g-C₃N₄ and FeP/g-C₃N₄ was the similar to that of NiFeP/g-C₃N₄ except for the addition of precursors.

2.5. Characterization methods

The X-ray diffraction (XRD) patterns of all samples were collected in the range 10–80° (2θ) using a RigakuD/MAX 2550 diffract meter (CuK radiation, $\lambda = 1.5406 \text{ \AA}$), operated at 40 kV and 100 mA. The morphologies were characterized by high resolution transmission electron microscopy (HRTEM, JEM2100). Elemental mapping was collected using a TEM (JEOL, JEM-2100F) equipped with EDX spectroscopy. The concentration of different metal ions were detected by ICP-AES (Agilent 725). The instrument employed for XPS studies was a Perkin-Elmer PHI 5000C ESCA system with Al K α radiation operated at 250 W. The shift of the binding energy due to relative surface charging was corrected using the C1s level at 284.6 eV as an internal standard. The UV-vis absorption was got from a UV-vis spectrophotometer (Varian, Cary 500) furnished with an integrating sphere assembly, using BaSO₄ as the reflectance sample. The photoluminescence spectra (PL) were carried out by a Hitachi F-4600 fluorescence spectrophotometer at room temperature and excited by an incident light of 360 nm. BET surface area measurements were carried out by N₂ adsorption at 77 K using an ASAP2020 instrument. The electrochemical impedance spectroscopy (EIS) and Photocurrent spectroscopy were all recorded on an electrochemical workstation (Zahner, Zennium). A standard three electrode system consisting of a working electrode that was prepared through a clean fluoride-tin oxide (FTO) deposited with a sample film, a Pt wire as the counter electrode and a saturated calomel electrode as the reference electrode in dark. The EIS measurements were performed in a 25 mmol/L K₃Fe(CN)₆ and K₄Fe(CN)₃ and 0.1 mol/L KCl mixture aqueous solution.

2.6. Photocatalytic measurements

To assess the photocatalytic performance of NiFeP/g-C₃N₄ materials, photocatalytic H₂ evolution reaction was measured in a 100 mL closed Pyrex reactor connected to a closed gas circulation and evacuation system under irradiation. For H₂ evolution, 100 mg catalyst was dispersed in 100 mL 10 vol.% triethanolamine (TEOA) aqueous solution. The 100 mL solution containing 90 mL water and 10 mL TEOA, the volume of the reactor is nearly 300 mL. The solution at the bottom of the reactor is surrounded by condensing circulating water of 5 °C. The

diameter of the reactor is 7.4 cm, the total irradiated area of the reactor is 42.9866 cm², the distance between light and the solution level is 8.3 cm, the deepness of solution is 3 cm. The system was vacuumized for 30 min to remove any residual air in solution before light irradiation. Photocatalytic H₂ evolution was then carried out by irradiating the solution using a 300 W Xenon lamp equipped with AM 1.5 air mass filter (simulated solar light irradiation). The gaseous product was analyzed by gas chromatography equipped with a thermal conductive detector (TCD) and a 5 Å molecular sieve column, using Argon as the carrier gas.

2.7. Degradation experimental procedure

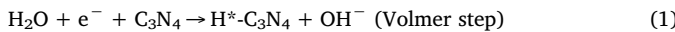
In a typical experiment of catalyst/PMS system, an aqueous solution of RhB (50 mL, 20 mg/L) was poured into a 50 mL photocatalytic tube, followed by the addition of a certain amount of PMS (1 mM) and catalyst (15 mg). During the reaction, the solution was irradiated with a 300 W Xenon lamp equipped with AM 1.5 air mass filter. During the reaction, samples were withdrawn using a dropper at predetermined time intervals and centrifuged to get the supernatant. The concentration of RhB was analyzed by using UV-vis spectrophotometer (Varian, Cary 500). In the catalyst/PMS/TEOA system, 10 vol.% TEOA was added as the hole scavenger (the whole system including 45 mL RhB solution and 5 mL TEOA). EPR measurement for in situ detection of ·OH/O₂⁻ was conducted using 5, 5-Dimethyl-1-Pyrrolidine-N-oxide (DMPO) as the spin-trapping agent in the aqueous and methanol media, respectively. [23–25] For the EPR measurement, the volume of each concentration test in EPR tests is 10 mL, the percentage of every material remains constant.

2.8. Computational details

First-principle calculations were performed using the all-electron code Fritz-Haber Institute *ab initio* molecules simulations package (FHI-aims) [26]. The exchange-correlation potentials were treated by the generalized gradient approximation (GGA) parameterized by Perdew, Burke, and Ernzerhof (PBE) [27,28]. The default “tight” species were used in this work. To account for the weak non-covalent intermolecular interaction, these functionals were augmented by the van der Waals scheme of Tkatchenko and Scheffler [29]. Periodic g-C₃N₄ monolayer was proposed to simulate the substrate, and the vacuum layer between neighboring models was at least 20 Å to reduce the electrostatic interactions between them. Brillouin zone was sampled using a 5 × 5 × 1 Monkhorst Pack k-point mesh during geometry optimization and single Gamma k-point for 3 × 3 × 1 supercell with phosphide nanoparticles deposited. Polarization effect was considered in all calculations.

2.9. Gibbs free energy of HER steps

In alkaline solution, the HER process is mainly composed of H* intermediates formation and H₂ formation [30], which could be represented as:



To avoid computing the exact free energy of OH⁻ in solutions, G_{OH⁻-e⁻} + G_{C₃N₄-H*} can be replaced by G_{C₃N₄-(H^{*}+OH^{*})} since the species H-OH is the ground state of water activation in Volmer step, and G_{OH⁻-e⁻} equals to G_{H₂O-1/2G_{H₂}} for Heyrovsky step. The free energies (at the reduction potentials U₀ = 0 V vs RHE) are calculated as:

$$\Delta G_1 = G_{\text{C}_3\text{N}_4-(\text{H}^*+\text{OH}^*)} - G_{\text{H}_2\text{O}} - G_{\text{C}_3\text{N}_4} \quad (4)$$

$$\Delta G_2 = G_{\text{C}_3\text{N}_4-\text{H}^*} - 1/2G_{\text{H}_2} - G_{\text{C}_3\text{N}_4} \quad (5)$$

2.10. Apparent quantum efficiency calculation

The apparent quantum efficiency (AQE) for 5NiFeP/g-C₃N₄ was measured under the same photocatalytic reaction condition except for the light source. The light source was 300 W Xenon lamp equipped with monochromatic mass filter at 365, 420, 475, 520, and 575 nm, respectively. The irradiation time was 3 h. The AQE was calculated using the following Eq. (6):

$$\text{AQE} = \frac{\text{Ne}}{\text{Np}} \times 100\% = \frac{2 \times M \times N_A \times h \times c}{S \times P \times t \times \lambda} \times 100\% \quad (6)$$

Ne: Number of reacted electrons; Np: Number of incident numbers; M: the amount of H₂; S: irradiation area; P: irradiation intensity; t: reaction time corresponding to the amount of H₂; λ: wavelength of the monochromatic light, N_A: Avogadro constant, h: Plank constant, c: the speed of light.

3. Results and discussion

3.1. Synthesis and structural morphology of NiFeP/g-C₃N₄

For our proof-of-concept studies, the compound of NiFeP and g-C₃N₄ were synthesized according to the detailed scheme in Fig. 1a. Firstly, the pristine g-C₃N₄ was prepared through a simple thermal polymerization by using melamine and ammonium chloride as the precursors. Then, the uniformly mixed aqueous solution of nickel-iron nitrate and hexamethylenetetramine were added to form NiFe(OH)₂ nanoparticles on g-C₃N₄ through chemical bath deposition. Eventually, the NiFeP/g-C₃N₄ was obtained using the CVD phosphorization of NiFe(OH)₂/g-C₃N₄ in a tube furnace. The X-ray diffraction (XRD) patterns of g-C₃N₄, NiFeP and 5NiFeP/g-C₃N₄ are clearly shown in Fig. 1b. Interestingly, the characteristic peaks of NiFeP (JCPDS card No. 54-1126) are not observed in the XRD pattern of 5NiFeP/g-C₃N₄, which is attributed to the relatively low concentration of NiFeP in the as-prepared compound. Two characteristic peaks of g-C₃N₄ are clearly shown at 13.0° and 27.4°, which can be associated with typical repeated in-plane tri-s-triazine and graphitic stacking of g-C₃N₄, respectively [31]. Additionally, the XRD patterns of g-C₃N₄ in all the as-prepared samples are also shown in Fig. S1. The optical properties of pristine g-C₃N₄, NiFeP nanoparticles, as well as all the as-prepared NiFeP/g-C₃N₄ samples were characterized with ultraviolet-visible (UV-vis) diffuse reflectance spectra (Fig. S2). The typical absorption edge at around 470 nm is observed in pristine g-C₃N₄. The corresponding color of NiFeP/g-C₃N₄ changes from yellow to dark gray with the increment of NiFeP, resulting in the enhanced absorption of NiFeP/g-C₃N₄ in the visible region, which is consistent with the results reported before [32]. Moreover, it should be noted that no apparent shift in the absorption edge of NiFeP/g-C₃N₄ is observed, ruling out that P atoms are not doped into the crystal lattice of g-C₃N₄.

Seen from Fig. 1c-e, high resolution transmission electron microscopy (HRTEM) and energy-dispersive X-ray spectroscopy (EDX) mapping confirmed the presence of NiFeP nanoparticles. The HRTEM image (Fig. 1c) clearly shows the highly dispersed distribution of obtained NiFeP nanoparticles on g-C₃N₄. The more detailed HRTEM image (Fig. 1d) shows two sets of distinct lattice fringes with the d-spacing of about 0.231 nm and 0.271 nm, corresponding to the (111) and (101) planes of NiFeP, respectively [7]. Notably, Energy-dispersive X-ray (EDX) analysis reveals the coexistence of C, N, Ni, Fe, and P (Fig. S3), and corresponding elemental mapping shows the uniform distribution of Ni, Fe, and P elements in NiFeP/g-C₃N₄ (Fig. 1e), indicating the successful combination of nickel-iron bimetallic phosphide and g-C₃N₄. Furthermore, the real contents of elements are measured and shown in Table S1, the accurate weight content of Ni and Fe in 5NiFeP/g-C₃N₄ is 1.4% and 1.3%, respectively. Besides, the calculated atom ratio of Ni and Fe is 1.02:1, which is the same with the theoretical adding ratio.

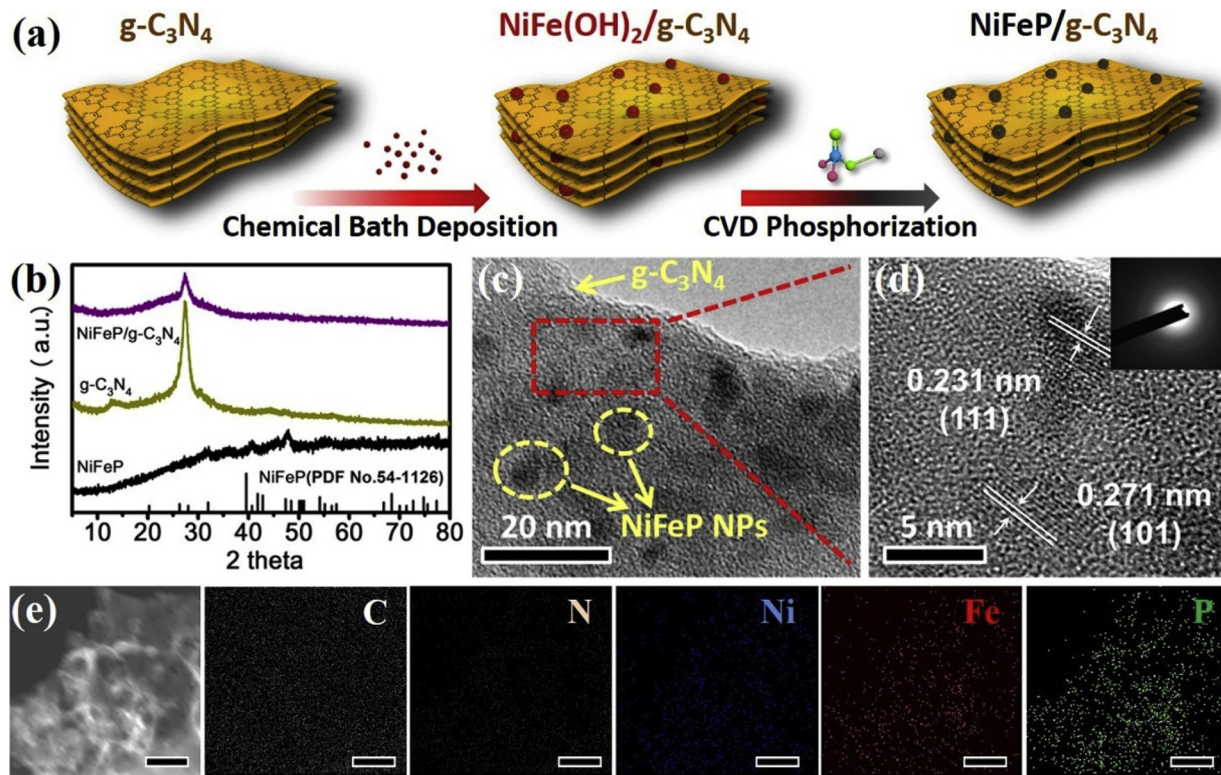


Fig. 1. (a) Schematic illustration of the fabrication process of $\text{NiFeP/g-C}_3\text{N}_4$. (b) XRD patterns of $\text{g-C}_3\text{N}_4$, $5\text{NiFeP/g-C}_3\text{N}_4$, NiFeP . (c, d) HRTEM images of $5\text{NiFeP/g-C}_3\text{N}_4$, and the inset in (d) is the corresponding SAED patterns. (e) HAADF-STEM image of $5\text{NiFeP/g-C}_3\text{N}_4$ and its corresponding element mapping images of C, N, Ni, Fe, P. The scale bar is 200 nm.

3.2. Surface chemical environment of photocatalyst and co-catalyst

To elucidate the surface chemical states and interaction effects between co-catalysts and $\text{g-C}_3\text{N}_4$, X-ray photoelectron spectroscopy (XPS) was conducted. XPS spectra in Fig. 2 reveal the existence of C, N, Ni, Fe, and P elements, which is consistent with the element mapping in Fig. 1e. The deconvolution of C 1s (Fig. 2a) had two peaks at 284.6 and 288.2 eV, corresponding to carbon in C–C bonds and N=C= [33,34]. The N 1s spectrum of $\text{g-C}_3\text{N}_4$ in Fig. 2b could be divided into three peaks at 398.68 eV, 400.65 eV, 404.37 eV, which can be assigned to nitrogen in C–N=C, N-(C)₃, and C-N-H, respectively [35]. Interestingly, the binding energy (BE) of C 1s and N 1s in $5\text{NiFeP/g-C}_3\text{N}_4$ both display a positive shift compared with $\text{g-C}_3\text{N}_4$ and single metal phosphide/ $\text{g-C}_3\text{N}_4$, attributing to the improved electron transfer ability from pristine $\text{g-C}_3\text{N}_4$ to bimetallic active sites, which is consistent with our previous work [36]. Further we compare the electronic environment of Ni and Fe in bimetallic phosphide with that in single metal phosphide. For the XPS peak fitting of Ni 2p, two main peaks with satellite peaks (marked as “Sat.”) and two very weak peaks at the binding energy of 853.1 eV and 870.4 eV can be identified in Fig. 2c. The peaks at 853.6 and 874.1 eV, along with their satellites, correspond to the Ni^{2+} arising from oxidation of Ni-PO_x owing to the exposure in the air [36]. Note that the BE at 853.1 eV and 870.4 eV can be assigned to partially positive charges Ni^{8+} in the NiFeP . The higher binding energy of Ni 2p in $\text{NiFeP/g-C}_3\text{N}_4$ indicates a stronger induced electron interaction with the addition of Fe. Meanwhile, the Fe 2p spectrum (Fig. 2d) shows the Fe 2p^{3/2} peak consists of two bands at 707.0 eV and 711.7 eV, and Fe 2p^{1/2} peak at 720.2 eV and 724.9 eV, corresponding to the Fe-P bonds and an Fe oxidation state [7]. Interestingly, the observation of negative shift in binding energy of Fe-P further proves that the increased electron density around Fe atoms along with the decreased electron density around Ni atoms, both of which indicate the existence of the felicitous electronic environments due to the synergistic effect between iron and

nickel atoms. The modulated electronic structure might be one possible reason to facilitate the HER performance. In Fig. S4, the XPS spectrum of P 2p shows three peaks at 129.3 eV, 130.8 eV, and 133.6 eV, corresponding to metal phosphides and the oxidized P species (P^{5+}), respectively. The binding energy at 129.3 eV is slightly lower than that of P^0 (130.0 eV), suggesting the existence of a strong bonding between metals with partially negative charged P^{8-} , which is consistent with the reported results [37]. Furthermore, the Brunauer–Emmett–Teller (BET) surface area of co-catalyst/ $\text{g-C}_3\text{N}_4$ is determined to be around $30 \text{ m}^2/\text{g}$ (Fig. S5), indicating the stability of $\text{g-C}_3\text{N}_4$ in the whole synthetic process. At the same time, we can also exclude the contribution of specific surface area to the HER activity.

3.3. Photocatalytic HER evaluation result

The photocatalytic hydrogen generation experiments were performed with triethanolamine (TEOA) as the sacrificial agent [38]. Control experiments showed no H_2 generation without $\text{g-C}_3\text{N}_4$ or light irradiation. Pristine $\text{g-C}_3\text{N}_4$ showed poor photocatalytic hydrogen evolution activity owing to its fast recombination of photo-generated electrons and holes [39]. Once co-catalysts were introduced onto $\text{g-C}_3\text{N}_4$, remarkable increase could be observed (Figs. 3a, b and S6, S7), among which NiFeP displayed the best HER performance. Bare NiFeP nanoparticles showed no activity towards HER under irradiation. This interesting result confirmed the great potential of NiFeP as an efficient bimetal co-catalyst towards HER, which guided our investigations further into the synergistic effect of nickel and iron concerned with thermodynamic regulation and promoted electronic transmission for efficient charge separation.

In order to further investigate the effect of NiFeP as a co-catalyst and improve the efficiency of hydrogen generation of $\text{g-C}_3\text{N}_4$, the loading amount of NiFeP on $\text{g-C}_3\text{N}_4$ was optimized. As shown in Figs. 3a, b and S6, gradually increasing the NiFeP content on $\text{g-C}_3\text{N}_4$

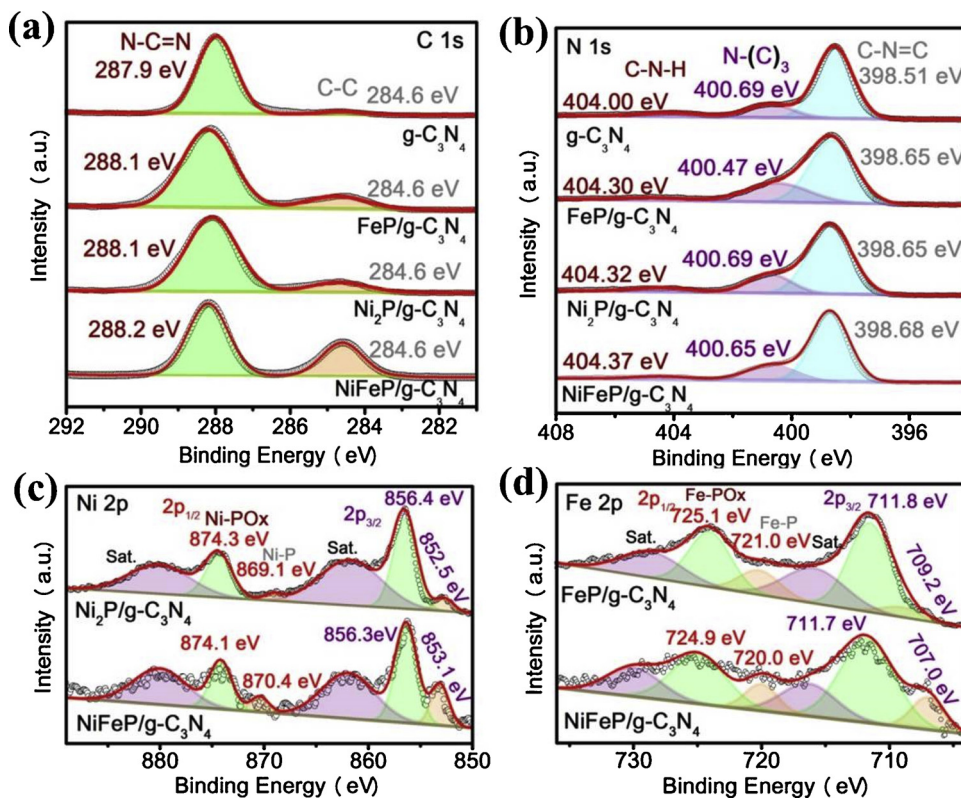


Fig. 2. Surface chemical states investigation of NiFeP/g-C₃N₄. XPS spectra of (a) C 1s, (b) N 1s, (c) Ni 2p, (d) Fe 1s in g-C₃N₄, 5Ni₂P/g-C₃N₄, 5FeP/g-C₃N₄, and 5NiFeP/g-C₃N₄.

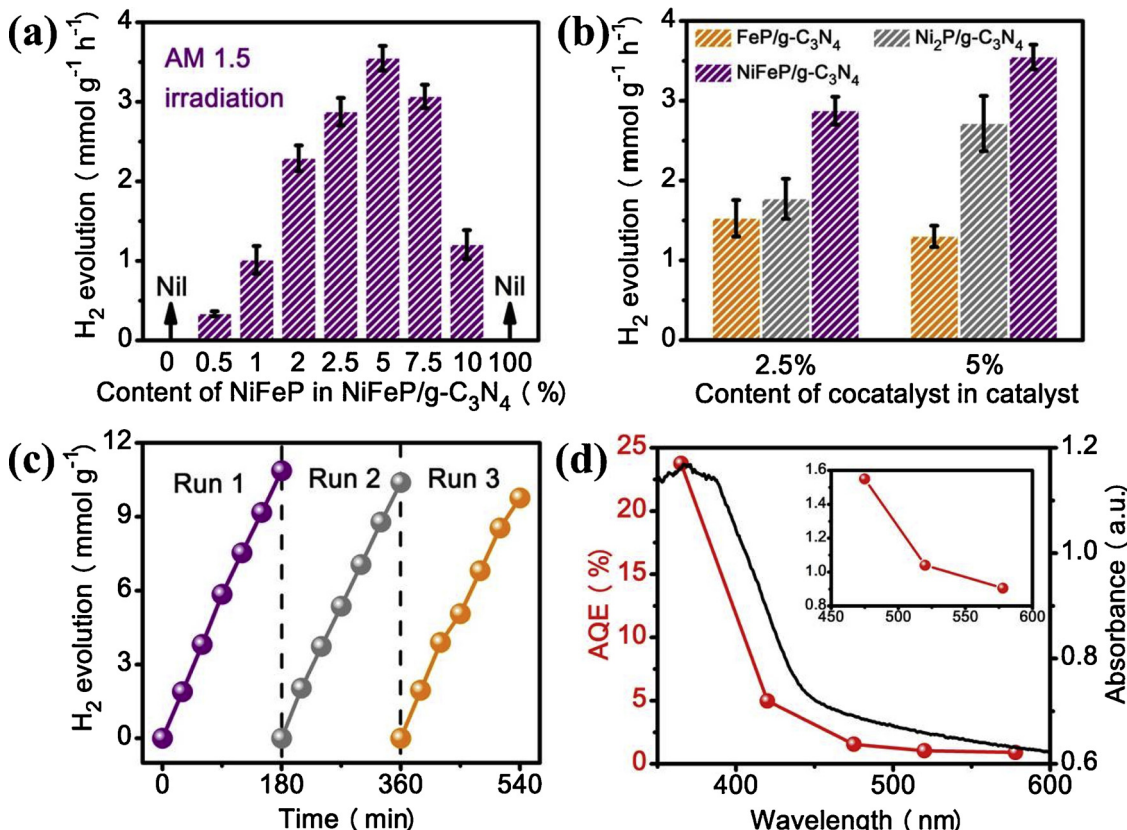


Fig. 3. (a) Photocatalytic hydrogen production rates of g-C₃N₄ and NiFeP/g-C₃N₄. (b) Photocatalytic hydrogen production rates of Ni₂P/g-C₃N₄, NiFeP/g-C₃N₄ and FeP/g-C₃N₄ (with the co-catalyst content is 2.5 wt% and 5 wt%). (c) Recyclability of hydrogen evolution tests of 5NiFeP/g-C₃N₄. (d) Wavelength-dependent quantum efficiency of hydrogen evolution activity over 5NiFeP/g-C₃N₄.

obviously improved the hydrogen generation activity due to the increased active sites. Notably, 5NiFeP/g-C₃N₄ exhibited the highest photocatalytic evolution rate of about 3.549 mmol g⁻¹ h⁻¹, which was higher than that of most reported co-catalyst/g-C₃N₄ (Table S2). However, further increasing the loading content of NiFeP to 10 wt% led to the decreasing hydrogen generation activity, which could be explained by the light-screening effect of excessive co-catalysts [40]. Besides, the turnover frequency (TOF) of 5NiFeP/g-C₃N₄ reached 10.4 h⁻¹, higher than those of 5Ni₂P/g-C₃N₄ (8.05 h⁻¹) and 5FeP/g-C₃N₄ (3.72 h⁻¹) (Fig. S8). Moreover, 5NiFeP/g-C₃N₄ remained changeless H₂ generation activity even after three cycles, indicating the sufficient stability of the structure and excellent electronic transmission capability of NiFeP towards H₂ generation (Fig. 3c). Importantly, seen from Fig. 3d, it could be clearly observed that the curve linked by the AQE values of 5NiFeP/g-C₃N₄ matches well with its absorption spectrum, and 5NiFeP/g-C₃N₄ achieves the quantum efficiency of 4.98% at 420 nm, which is superior than that of most reported co-catalyst/g-C₃N₄ (Table S3). From the above discussion, it can be found that enabled by the doping of Fe atoms into Ni₂P structure, the increased active sites and the modulated electronic structure of bimetallic phosphide can largely facilitate the HER performance as compared to single metallic phosphide.

3.4. Electronic transmission discussion

To further investigate deeper into the direct electron migration pathway, we first need to eliminate the influence of co-catalyst on the band structure of g-C₃N₄. The derived bandgaps, the valence band (VB) positions, and the conduction band (CB) positions of pristine g-C₃N₄, 5Ni₂P/g-C₃N₄, 5FeP/g-C₃N₄, and 5NiFeP/g-C₃N₄ are shown in Figs. S9–S12, indicating the introduction of co-catalysts does not largely influence the bandgap of g-C₃N₄. The bandgap of the four as-prepared samples were derived from UV-vis spectra (inset of Fig. S9), which are 2.82 eV, 2.72 eV, 2.72 eV, and 2.66 eV for g-C₃N₄, 5FeP/g-C₃N₄, 5Ni₂P/g-C₃N₄, and 5NiFeP/g-C₃N₄, respectively. The VB of g-C₃N₄, 5FeP/g-C₃N₄, 5Ni₂P/g-C₃N₄, and 5NiFeP/g-C₃N₄ were determined from the XPS valence band spectra (Fig. S10), indicating the VB positions of all the four samples are located at 2.01 eV. Furthermore, according to the Mott-Schottky tests (Fig. S11), the CB potential of g-C₃N₄, 5FeP/g-C₃N₄, 5Ni₂P/g-C₃N₄, and 5NiFeP/g-C₃N₄ is -0.81 eV, -0.71 eV, -0.71 eV, and -0.65 eV, respectively. Combining the derived bandgap, VB and CB together (Fig. S12), it can be observed that the introduction of co-catalysts does not largely influence the bandgap of g-C₃N₄. Then, photoelectrochemical (PEC) measurements were applied to study the behaviors of the photogenerated electrons and holes. Compared with 5Ni₂P/g-C₃N₄ and 5FeP/g-C₃N₄, 5NiFeP/g-C₃N₄ showed an enhanced photocurrent (Figs. 4a and S13), testifying an enhanced charge separation efficiency with NiFeP co-catalyst. The electrochemical impedance spectroscopy (EIS) Nyquist plot in Fig. 4b showed a remarkable decrease in the arc radius for 5NiFeP/g-C₃N₄, which reflects a lower interfacial charge transfer resistance with bimetallic phosphides. For the deeper study of the charge transfer properties in bimetallic co-catalyst, steady-state and time-resolved spectroscopic techniques were applied to further investigate during the whole photocatalytic process. Photoluminescence (PL) spectra were acquired at an excitation wavelength of 370 nm at room temperature (Figs. 4c and S14). The PL intensity of g-C₃N₄ was significantly diminished after the introduction of co-catalysts, and NiFeP with a modulated electronic structure showed the lowest intensity, suggesting the effective suppressed recombination of photogenerated electrons and holes. Furthermore, the fluorescent lifetime of g-C₃N₄ was decayed from ~8.77 ns (g-C₃N₄) to ~7.04 ns (Ni₂P/g-C₃N₄), 8.16 ns (FeP/g-C₃N₄), even 5.21 ns (NiFeP/g-C₃N₄) (Fig. 4d and Table 1). On the surface, the lifetime of photogenerated carriers of catalyst is contradictory to its HER activity. It looks strange that the sample (5NiFeP/g-C₃N₄) with the highest H₂ production yield had the shortest carrier lifetime. However,

if we fit the lifetime of photogenerated carriers into “τ1”, “τ2” and “τ3”, it is not difficult to understand the above mentioned “contradictory”. “τ1” represents the fluorescence decay time of the excited electrons from the conduction band to the valence band of bulk g-C₃N₄. “τ2” is the fluorescence decay time of the recombination of photo-generated electron-hole pairs on the surface of g-C₃N₄ [41]. “τ3” is assigned to the fluorescence decay time of the recombination of photo-generated electron-hole pairs on the co-catalyst of NiFeP, Ni₂P or FeP [42]. Interestingly, the lifetime of surface carriers on g-C₃N₄ (τ2) was significantly shortened after the loading of co-catalyst. Meanwhile, the lifetime of surface carriers on co-catalyst (τ3) is obviously longer than that of bulk carriers in g-C₃N₄ (τ1). It is indicated that most of the photogenerated carriers of g-C₃N₄ are directionally transferred to the co-catalyst surface. As the delocalization capacity of electrons on the surface of the co-catalyst is worse than that of the electrons on the surface of g-C₃N₄, leading to the short lifetime of the carrier on the whole catalyst of NiFeP/g-C₃N₄ (τ). Although the photo-generated electrons on the co-catalyst are more localized, they are more likely to react with the protons trapped on the co-catalyst to give off hydrogen [43].

To further confirm the localization capacity of photo-generated electrons over the co-catalyst of NiFeP, the experiment of decomposition of PMS for the degradation of RhB was carried out in our case, as shown in Fig. 4e. The degradation phenomenon with PMS as an oxidant help us to further understand the electron trapping role of the bimetallic phosphides. In previous report, PMS could be activated to form sulfate radical (SO₄^{·-}) by alkaline, activated carbon, light, ultrasound and so on [44–48]. In the degradation system with PMS, all kinds of intermediates including free radicals and ions (HSO₅^{·-}, SO₄²⁻, SO₅²⁻, HSO₄^{·-}, SO₄²⁻, ·OH, O₂^{·-}) will emerge and interconvert at any time [44]. Our experiments included two steps, the first step is the degradation of RhB by pure catalysts and PMS, the only change in the second step is just adding TEOA as the hole sacrificial agent to further detect the performance of photo-excited electrons while other solution conditions are the same. Different from the HER performance, the activity of g-C₃N₄ for the RhB degradation was not significantly improved after the loading of co-catalyst of NiFeP. Interestingly, the activity of 5NiFeP/g-C₃N₄ for the RhB degradation was lower than that of the pure g-C₃N₄, after the addition of TEOA. It indicates that these two photocatalytic systems have different mechanisms for the decomposition of PMS to produce reactive oxygen species (ROS). Firstly, the formation of hydroxyl radicals (·OH) [49] in different photocatalytic systems were detected, as shown in Fig. 4f. In the system of g-C₃N₄ + PMS, only ·OH was generated but no EPR signal peak of sulfate radical (SO₄^{·-}) [50] was found, indicating that PMS basically did not decompose under the simulated solar light [51]. And the ·OH should be induced by the photo-generated holes from g-C₃N₄ (Eqs. 7 and 8). [52] Interestingly, after loading the co-catalyst of NiFeP, the EPR spectrum of 5NiFeP/g-C₃N₄ shows the signal peaks of SO₄^{·-}, indicating the photo-generated electrons over 5NiFeP/g-C₃N₄ are used to decompose the PMS (Eq. 9). As a hole sacrificial agent, TEOA has a certain reducibility, which also can consume ·OH and SO₄^{·-}. Therefore, after adding of TEOA in the systems, all the EPR signals of radicals are disappearing. Another interesting finding is that the g-C₃N₄ + PMS + TEOA still has the activity for the degradation of RhB, although no strong oxidizing ·OH was detected in the reaction system (Fig. 4e). It means that the photogenerated electrons and their derivatives may be at work. The EPR was also employed to detect the formation of superoxide radicals (O₂^{·-}) [53] in our case, as shown in Fig. 4g. Although TEOA was added to the system, O₂^{·-} could still be observed over g-C₃N₄ + PMS + TEOA, suggesting that the photogenerated electrons migrated on the surface of g-C₃N₄ can react with O₂ to produce O₂^{·-} (Eq. 10). And the ·OH and O₂^{·-} are responsible for the degradation of RhB in g-C₃N₄ + PMS system (Eq. 11). Differently, after loading of NiFeP, the corresponding EPR signals of O₂^{·-} over 5NiFeP/g-C₃N₄ + PMS are very weak. However, as can be seen from the above results of the photocurrent and fluorescence characterization

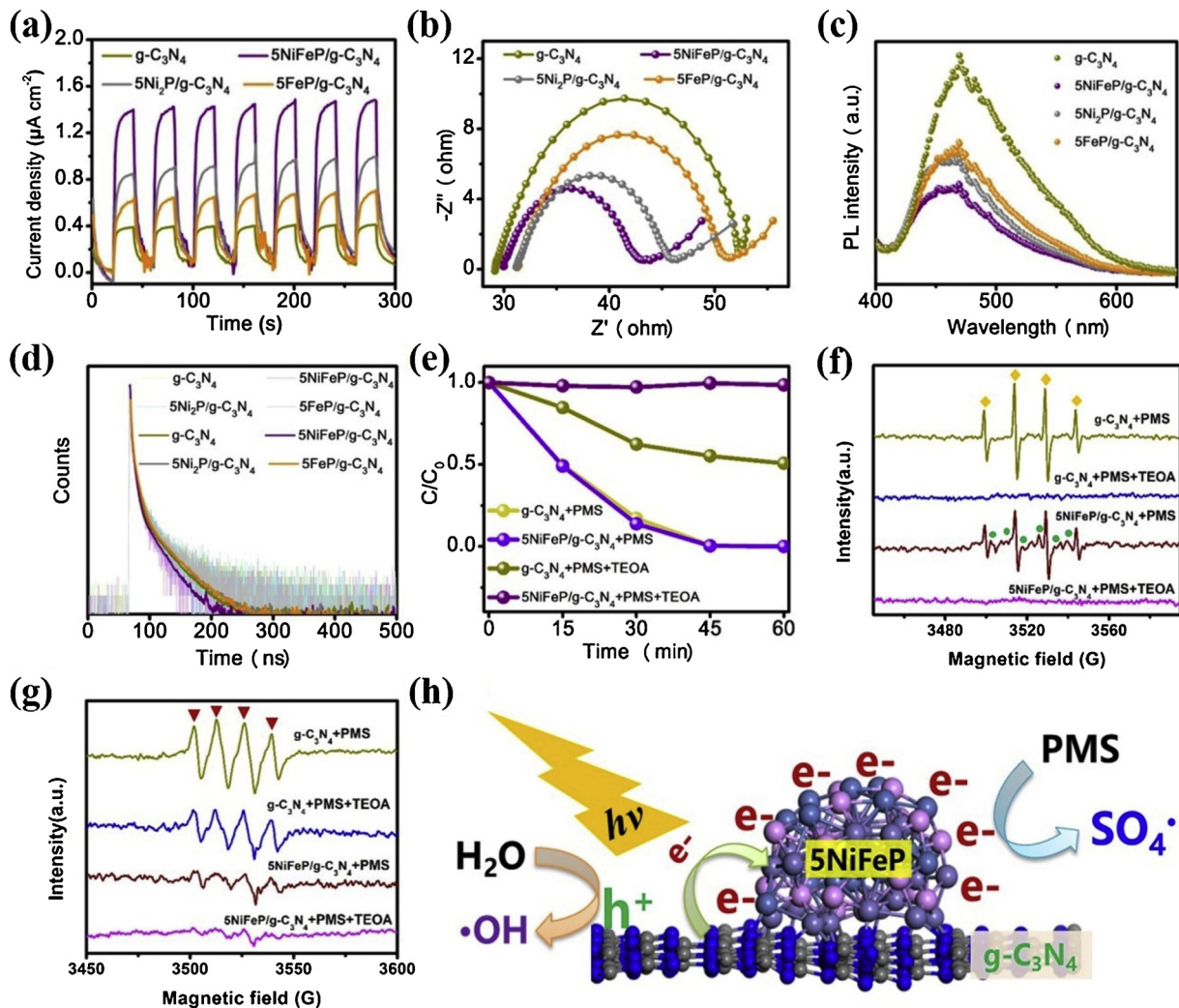


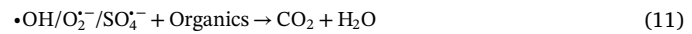
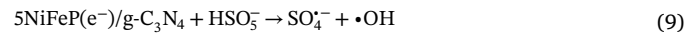
Fig. 4. Investigation of photo-generated electrons migration. (a) Transient photocurrent plots, (b) EIS Nyquist plots, (c) Photoluminescence spectra (at an excitation wavelength of 370 nm), and (d) Time-resolved Fluorescence decay spectra of the as-prepared samples: g-C₃N₄, 5NiFeP/g-C₃N₄, 5Ni₂P/g-C₃N₄, 5FeP/g-C₃N₄. (e) Degradation of RhB in the catalyst/PMS system and catalyst/PMS/TEOA system under simulated solar light. Spin-trapping EPR spectra for (f) ·OH and (g) O₂^{·-} in catalyst/PMS/TEOA system (“yellow diamonds”, “green circles” and “inverted triangles” are ascribed to ·OH, SO₄²⁻ and O₂^{·-}, respectively). (h) Illustration of electron directed migration over 5NiFeP/g-C₃N₄/PMS system under light irradiation. (For interpretation of the references to colour in this figure legend, the reader is referred to the web version of this article.)

Table 1

Kinetic parameters of time-resolved fluorescence decays of g-C₃N₄, 5NiFeP/g-C₃N₄, 5Ni₂P/g-C₃N₄, 5FeP/g-C₃N₄ under 470 nm excitation.

Sample	τ ₁ /ns	τ ₂ /ns	τ ₃ /ns	τ/ns
g-C ₃ N ₄	4.02(81.58%)	29.80(18.42%)		8.77
5NiFeP/g-C ₃ N ₄	0.84(53.26%)	4.47(34.78%)	26.86(11.96%)	5.21
5Ni ₂ P/g-C ₃ N ₄	1.57(59.97%)	7.08(29.72%)	38.74(10.31%)	7.04
5FeP/g-C ₃ N ₄	1.45(52.23%)	6.84(34.29%)	37.54(13.48%)	8.16

(Fig. 4a, c), the concentration of photogenerated electron has an obvious increase after the introduction of co-catalyst. Therefore, we can infer that the photogenerated electrons directionally migrate from g-C₃N₄ to NiFeP. Those electrons’ delocalization capacities are too poor to react with O₂. On the other hand, transition metal atoms (Ni or Fe) are more likely to bond with PMS molecules [54], so their surface electrons are more likely to decompose PMS. Thus, it can be concluded that the photogenerated holes over 5NiFeP/g-C₃N₄ are mainly concentrated on the surface of g-C₃N₄ to decompose H₂O for the generation of ·OH, while the photogenerated electrons are directed to the NiFeP to react with the neighboring PMS or protons to form SO₄²⁻ or H₂ (Fig. 4h).



The calculated local charge density difference of NiFeP/g-C₃N₄ in Fig. 5a demonstrates that the electrons density of H atoms is nearly 0.35e⁻, further confirming the electron trapping ability of co-catalysts. Besides, to shed more light on the synergistic effect of the bimetallic active center in NiFeP based on g-C₃N₄ and compare HER in thermodynamic, DFT calculations were performed for the key reaction steps. As shown in Figs. 5b and S15, the reaction pathway for hydrogen evolution reaction in alkaline environment, including the absorption of water (step 1), water dissociation (step 2), the formation of H^{*} intermediate (step 3), and hydrogen evolution (step 4), was designed [55,56]. The absolute value of free energy, |ΔG_{H*}|, had been used as a major descriptor of the HER activity for a wide variety of complex catalysts [57]. And the |ΔG_{H*}| of highly efficient catalyst should be

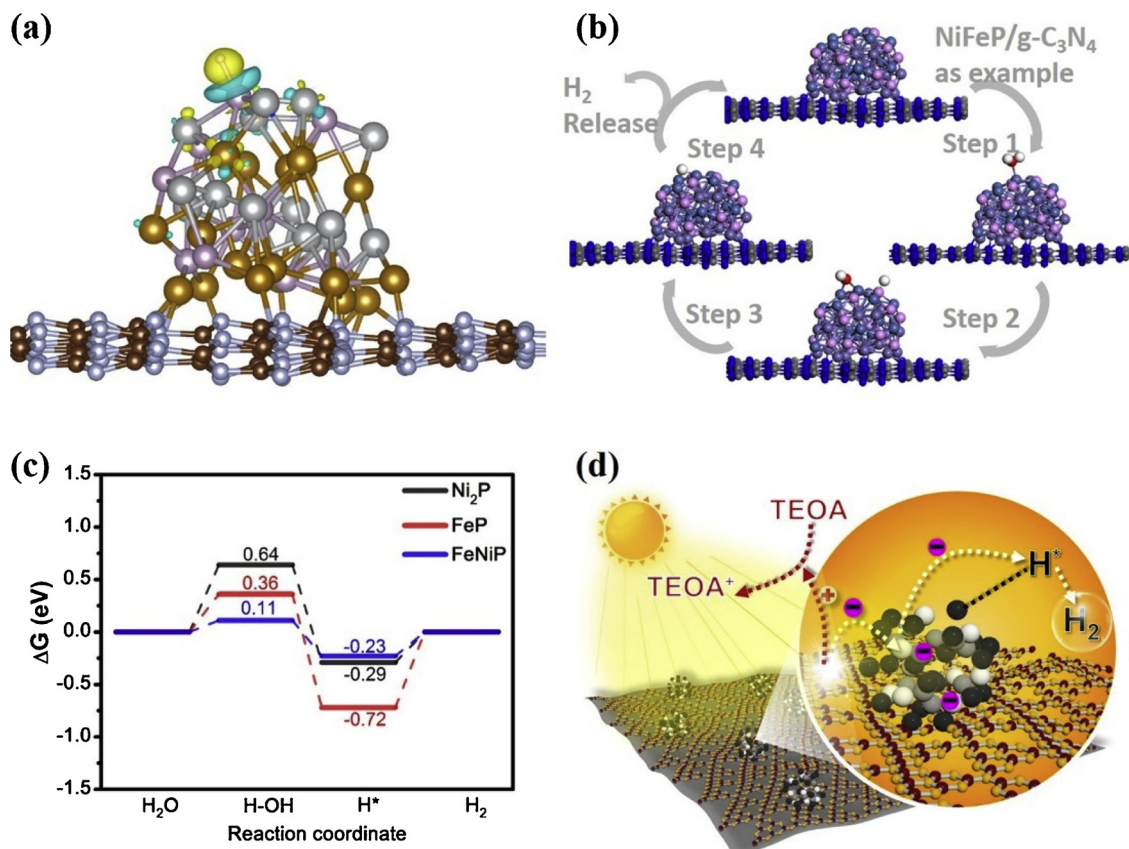


Fig. 5. Thermodynamic regulation over NiFeP/g-C₃N₄ for photocatalytic HER. (a) Local charge density difference of NiFeP/g-C₃N₄ (yellow and cyan are 0.001 e per Å³ isosurfaces; silver gray spheres: Ni atoms; brown spheres: Fe atoms; pink spheres: P atoms; white spheres: H atoms; coffee spheres: C atoms; sky blue spheres: N atoms). (b) Water adsorption models on the surface of NiFeP/g-C₃N₄ (Purple spheres: Fe atoms; dark blue spheres: Ni atoms; pink spheres: P atoms; blue spheres: N atoms; gray spheres: C atoms; white spheres: H atoms). (c) Free energy diagrams for H₂O reduction to H₂ by the thermochemical model on Ni₂P, Fe₂P, and NiFeP surface. (d) Mechanism diagram in the NiFeP/g-C₃N₄ system for the photocatalytic HER. (For interpretation of the references to colour in this figure legend, the reader is referred to the web version of this article.)

close to zero eV. The binding free energy (ΔG_{H^*}) diagrams of Ni₂P, Fe₂P, and NiFeP in the reaction are shown in Fig. 5c. The ΔG_{H^*} value is -0.29 eV for the single metal co-catalyst Ni₂P, which is obviously close to the optimal value (ΔG_{H^*} is close to zero eV). Nevertheless, Ni₂P expresses an unsatisfactory catalyst-OH_{ad} free energy (ΔG_{H2O}), which is up to 0.64 eV. The water dissociation is impeded and the hydrogen evolution is reduced with the high ΔG_{H2O} [55]. Compared with Ni₂P, Fe₂P exhibits lower ΔG_{H2O} , indicating a faster dissociation of H₂O. Unfortunately, the ΔG_{H^*} of Fe₂P is -0.72 eV, the calculated high $|\Delta G_{H^*}|$ of Fe₂P is consistent with the experimental results of hydrogen evolution in our work. However, the ΔG_{H2O} value for our NiFeP/g-C₃N₄ was 0.11 eV and the ΔG_{H^*} value for the NiFeP/g-C₃N₄ was about -0.23 eV, which was a clear demonstration of its best catalytic activity from the free energy diagrams. In this way, the introduction of Fe atoms into Ni₂P on the interface of NiFeP/g-C₃N₄ leads to optimized adsorption energy of the intermediates, which boosts the HER performance of NiFeP/g-C₃N₄ in the alkaline environment, agreeing well with the experimental observations. In general, our DFT calculations together with degradation of RhB (PMS decomposition), confirm the electron directed migration from the g-C₃N₄ to the electron deficient bimetallic center and the reduced energy barriers (ΔG_{H2O} and ΔG_{H^*}), which can both largely facilitate the HER performance (Fig. 5d).

Furthermore, we carried out DFT calculations to confirm the photogenerated electron migration pathway. As shown in Fig. S16, the density of state intensity at Fermi level is non-zero, which indicates a metallic nature of NiFeP, thus in favor of the electron transfer in catalysis. When NiFeP contacts with g-C₃N₄, a Schottky junction is formed at the metal-semiconductor (NiFeP-g-C₃N₄) interface. The difference in

Fermi levels between NiFeP and g-C₃N₄ drives the charge flow propagated by electrons or holes until the system reaches equilibrium, followed by conduction band bending of g-C₃N₄ and Schottky barrier formation (Fig. S17). The Schottky barrier has been regarded as photogenerated-electron trap [58,59]. Based on these consideration, the photo-electrons migration direction is from g-C₃N₄ to NiFeP.

4. Conclusion

In summary, we developed an outstanding bimetallic phosphides NiFeP to realize the improved HER activity of g-C₃N₄, with the help of direct electron migration from g-C₃N₄ to bimetallic active sites. Meanwhile, the doping of Fe atoms into Ni₂P structure can not only modulate the electronic structure, but also contribute largely to the reduced energy barriers (ΔG_{H2O} and ΔG_{H^*}), thus accelerating the HER activity. The cooperation of experimental and theoretical investigations demonstrates the enhanced alkaline HER kinetics of NiFeP/g-C₃N₄ for the H₂ generation performance. Besides, the distribution of electrons on the surface of NiFeP is confirmed by measuring the lifetime of photogenerated carriers and the degradation tests with the help of PMS. Furthermore, the photogenerated electron migration pathway is further confirmed via the calculated DOS from DFT calculations. This work about bimetallic phosphides clearly reveals the electron directed migration pathway in co-catalyst/g-C₃N₄ photocatalytic HER system, and provides theoretical guidance for the design and preparation of multi-metallic center photocatalytic system with a higher HER activity in the future.

Author contributions

Q.Z. and M.X. conceived and designed the research. Q.Z. synthesized photocatalysts and conducted all the experiments. H.D. carried out the theoretical calculations. Q.Z. and M.X. wrote the paper. J.Z. gave suggestions on the experiment and writing. All authors discussed and analyzed the data.

Declaration of Competing Interest

The authors declare no competing financial interest.

Acknowledgments

This work was supported by National Natural Science Foundation of China (5171101651, 21822603, 21811540394, 21677048, 21773062, 21577036), the State Key Research Development Program of China (2016YFA0204200), Shanghai Pujiang Program (17PJD011), the Fundamental Research Funds for the Central Universities (22A201514021, 50321101915005) and Science and Technology Commission of Shanghai Municipality (16JC1401400, 17520711500). This Project was supported by Shanghai Municipal Science and Technology Major Project (Grant No. 2018SHZDZX03) and the Programme of Introducing Talents of Discipline to Universities (B16017). The authors thank Research Center of Analysis and Test of East China University of Science and Technology for the help on the characterization.

Appendix A. Supplementary data

Supplementary material related to this article can be found, in the online version, at doi:<https://doi.org/10.1016/j.apcatb.2019.118078>.

References

- [1] L. Bi, X. Gao, L. Zhang, D. Wang, X. Zou, T. Xie, *ChemSusChem* 11 (2018) 276–284.
- [2] B. Qiu, L. Cai, Y. Wang, Z. Lin, Y. Zuo, M. Wang, Y. Chai, *Adv. Funct. Mater.* 28 (2018) 1706008.
- [3] H. Wang, Y. Hsu, R. Chen, T. Chan, H. Chen, B. Liu, *Adv. Energy Mater.* 5 (2015) 1500091.
- [4] B. Qiu, C. Wang, N. Zhang, L. Cai, Y. Xiong, Y. Chai, *ACS Catal.* 9 (2019) 6484–6490.
- [5] B.D. Yuhas, A.L. Smeigh, A.P. Douvalis, M.R. Wasielewski, M.G. Kanatzidis, *J. Am. Chem. Soc.* 134 (2012) 10353–10356.
- [6] H. Huang, C. Yu, C. Zhao, X. Han, J. Yang, Z. Liu, S. Li, M. Zhang, J. Qiu, *Nano Energy* 34 (2017) 472–480.
- [7] M. Qian, S. Cui, D. Jiang, L. Zhang, P. Du, *Adv. Mater.* 29 (2017) 1704075.
- [8] B. Qiu, L. Cai, Y. Wang, S. Ma, Y.H. Tsang, Y. Chai, *Mater. Today Energy* 11 (2019) 89–96.
- [9] X. Jia, Y. Zhao, G. Chen, L. Shang, R. Shi, X. Kang, G.I. Waterhouse, L.Z. Wu, C.H. Tung, T. Zhang, *Adv. Energy Mater.* 6 (2016) 1502585.
- [10] X. Long, G. Li, Z. Wang, H. Zhu, T. Zhang, S. Xiao, W. Guo, S. Yang, *J. Am. Chem. Soc.* 137 (2015) 11900–11903.
- [11] C.G. Morales-Guio, L.-A. Stern, X. Hu, *Chem. Soc. Rev.* 43 (2014) 6555–6569.
- [12] Z.W. Seh, J. Kibsgaard, C.F. Dickens, I. Chorkendorff, J.K. Nørskov, T.F. Jaramillo, *Science* 355 (2017) eaad4998.
- [13] J. Greeley, T.F. Jaramillo, J. Bonde, I. Chorkendorff, J.K. Nørskov, *Nat. Mater.* 5 (2006) 909.
- [14] Y. Shi, B. Zhang, *Chem. Soc. Rev.* 45 (2016) 1529–1541.
- [15] B. Qiu, M. Xing, J. Zhang, *Chem. Soc. Rev.* 47 (2018) 2165–2216.
- [16] Y. Xin, X. Kan, L. Gan, Z. Zhang, *ACS Nano* 11 (2017) 10303–10312.
- [17] Z. Huang, J. Song, K. Li, M. Tahir, Y. Wang, L. Pan, L. Wang, X. Zhang, J. Zou, *J. Am. Chem. Soc.* 138 (2016) 1359–1365.
- [18] J. Ran, G. Gao, F. Li, T. Ma, A. Du, S. Qiao, *Nat. Commun.* 8 (2017) 13907.
- [19] Z. Peng, J. Lai, Y. Tang, Y. Chao, F. Lin, S. Guo, *Appl. Catal. B: Environ.* 238 (2018) 161–167.
- [20] J. Xu, Y. Qi, C. Wang, L. Wang, *Appl. Catal. B: Environ.* 241 (2019) 178–186.
- [21] X. Gao, X. Li, W. Yu, *J. Phys. Chem. B* 109 (2005) 1155–1161.
- [22] B. Qiu, Q. Zhu, M. Xing, J. Zhang, *Chem. Commun.* 53 (2017) 897–900.
- [23] Y. Ye, C. Shan, X. Zhang, H. Liu, D. Wang, L. Lv, B. Pan, *Environ. Sci. Technol.* 52 (2018) 10657–10664.
- [24] M. Ou, S. Wan, Q. Zhong, S. Zhang, Y. Song, L. Guo, W. Cai, Y. Xu, *Appl. Catal. B: Environ.* 221 (2018) 97–107.
- [25] É. Hideg, Z. Deák, M. Hakala-Yatkin, M. Karonen, A.W. Rutherford, E. Tyystjärvi, I. Vass, A. Krieger-Liszskay, *BBA – Bioenergetics* 1807 (2011) 1658–1661.
- [26] V. Blum, R. Gehrke, F. Hanke, P. Havu, V. Havu, X. Ren, K. Reuter, M. Scheffler, *Comput. Phys. Commun.* 180 (2009) 2175–2196.
- [27] J.P. Perdew, K. Burke, M. Ernzerhof, *Phys. Rev. Lett.* 77 (1996) 3865.
- [28] G. Kresse, D. Joubert, *Phys. Rev. B* 59 (1999) 1758.
- [29] A. Tkatchenko, M. Scheffler, *Phys. Rev. Lett.* 102 (2009) 073005.
- [30] B. Zhang, J. Liu, J. Wang, Y. Ruan, X. Ji, K. Xu, C. Chen, H. Wan, L. Miao, J. Jiang, *Nano Energy* 37 (2017) 74–80.
- [31] N. Meng, J. Ren, Y. Liu, Y. Huang, T. Petit, B. Zhang, *Energy Environ. Sci.* 11 (2018) 566–571.
- [32] L. Bi, X. Gao, L. Zhang, D. Wang, X. Zou, T. Xie, *ChemSusChem* 11 (2018) 276–284.
- [33] J. Zhang, M. Zhang, G. Zhang, X. Wang, *ACS Catal.* 2 (2012) 940–948.
- [34] B. Qiu, Y. Deng, Q. Li, B. Shen, M. Xing, J. Zhang, *J. Phys. Chem. C* 120 (2016) 12125–12131.
- [35] C. Li, Y. Du, D. Wang, S. Yin, W. Tu, Z. Chen, K. Markus, G. Chen, R. Xu, *Adv. Funct. Mater.* 27 (2017) 1604328.
- [36] Q. Zhu, B. Qiu, M. Du, M. Xing, J. Zhang, *Ind. Eng. Chem. Res.* 57 (2018) 8125.
- [37] M. Qian, S. Cui, D. Jiang, L. Zhang, P. Du, *Adv. Mater.* 29 (2017) 1704075.
- [38] Y. Chen, Z. Zhan, J. Wang, Y. Shen, S. Liu, Y. Zhang, *Chin. Chem. Lett.* 29 (2018) 437–440.
- [39] W. Iqbal, B. Qiu, Q. Zhu, M. Xing, J. Zhang, *Appl. Catal. B: Environ.* 232 (2018) 306–313.
- [40] Q. Guo, F. Liang, X. Gao, Q. Gan, X. Li, J. Li, Z. Lin, C. Tung, L. Wu, *ACS Catal.* (2018) 5890–5895.
- [41] P. Zhang, M. Fujitsuka, T. Majima, *J. Energy Chem.* 25 (2016) 917–926.
- [42] L. Lin, C. Hou, X. Zhang, Y. Wang, Y. Chen, T. He, *Appl. Catal. B: Environ.* 221 (2018) 312–319.
- [43] K. Chang, Z. Mei, T. Wang, Q. Kang, S. Ouyang, J. Ye, *ACS Nano* 8 (2014) 7078–7087.
- [44] J. Wang, S. Wang, *Chem. Eng. J.* 334 (2018) 1502–1517.
- [45] J. Fan, H. Qin, S. Jiang, *Chem. Eng. J.* 359 (2019) 723–732.
- [46] W. Qin, G. Fang, Y. Wang, D. Zhou, *Chem. Eng. J.* 348 (2018) 526–534.
- [47] J. Zou, J. Ma, L. Chen, X. Li, Y. Guan, P. Xie, C. Pan, *Environ. Sci. Technol.* 47 (2013) 11685–11691.
- [48] L. Ling, D. Zhang, C. Fan, C. Shang, *Water Res.* 124 (2017) 446–453.
- [49] M. Xing, W. Xu, C. Dong, Y. Bai, J. Zeng, Y. Zhou, J. Zhang, Y. Yin, *Chem* 4 (2018) 1359–1372.
- [50] T. Zeng, H. Zhang, Z. He, J. Chen, S. Song, *Sci. Rep.* 6 (2016) 33348.
- [51] M. Xie, J. Tang, L. Kong, W. Lu, V. Natarajan, F. Zhu, J. Zhan, *Chem. Eng. J.* 360 (2019) 1213–1222.
- [52] Y. Wang, L. Bai, Z. Zhang, Y. Qu, L. Jing, *Res. Chem. Intermed.* 45 (2019) 249–259.
- [53] D. Dvoranová, Z. Barbierková, M. Mazúř, E.I. García-López, G. Marci, K. Lušpá, V. Brezová, *J. Photoch. Photobio. A* 375 (2019) 100–113.
- [54] X. Li, X. Huang, S. Xi, S. Miao, J. Ding, W. Cai, S. Liu, X. Yang, H. Yang, J. Gao, J. Wang, Y. Huang, T. Zhang, B. Liu, *J. Am. Chem. Soc.* 140 (2018) 12469–12475.
- [55] B. Zhang, J. Liu, J. Wang, Y. Ruan, X. Ji, K. Xu, C. Chen, H. Wan, L. Miao, J. Jiang, *Nano Energy* 37 (2017) 74–80.
- [56] J. Zhang, T. Wang, P. Liu, S. Liu, R. Dong, X. Zhuang, M. Chen, X. Feng, *Energy Environ. Sci.* 9 (2016) 2789–2793.
- [57] J.K. Nørskov, T. Bligaard, A. Logadottir, J. Kitchin, J.G. Chen, S. Pandelov, U. Stimming, *J. Electrochem. Soc.* 152 (2005) J23–J26.
- [58] Z. Zhuang, Y. Li, Z. Li, F. Lv, Z. Lang, K. Zhao, L. Zhou, L. Moskaleva, S. Guo, L. Mai, *Angew. Chem. Int. Ed.* 57 (2018) 496–500.
- [59] J. Lee, S. Mubeen, X. Ji, G.D. Stucky, M. Moskovits, *Nano Lett.* 12 (2012) 5014–5019.